THE ASTROPHYSICAL JOURNAL, 456:152–162, 1996 January 1

HIGH-RESOLUTION *IRAS* MAPS AND INFRARED EMISSION OF M31. I. MORPHOLOGY AND SOURCES

CONG XU
Max-Planck-Institut für Kernphysik, Postfach 103980, 69117 Heidelberg, Germany
AND
GEORGE HELOU
IPAC 100-22, California Institute of Technology, Pasadena, CA 91125
Received 1994 May 9; accepted 1995 July 6

ABSTRACT

The morphology of the infrared (IR) emission and the properties of discrete far-infrared (FIR) sources in the M31 disk are studied using the high-resolution (HiRes) maps from *IRAS*. Very thin and bright FIR arm segments are shown in these maps, which have similar structure as the H I gas but with much enhanced arm/interarm contrast, typically a factor of ~ 5 on the 60 μm image. We identify 39 unconfused sources (excluding the nucleus) and 14 confused sources (seven pairs) at 60 μm by direct Gaussian fittings to the image. *IRAS* colors of 10 bright isolated sources are studied, which are presumably representative of the discrete sources in general. The colors follow the well-known anticorrelation between $f_{60\,\mu m}/f_{100\,\mu m}$ and $f_{12\,\mu m}/f_{25\,\mu m}$. All sources coincide with optical H II regions. A comparison with Hα observations shows that the total luminosity (in the wavelength range 8–1000 μm) associated with H II regions is $7.2 \pm 2.9 \times 10^8\ L_\odot$, namely, 30% $\pm$ 14% of the total IR emission of M31. Half the IR luminosity of this component emerges from the sources. This luminosity translates into a present-day star formation rate of $0.36 \pm 0.14\ M_\odot\ \mathrm{yr}^{-1}$, about an order of magnitude lower than that of the Milky Way.

Subject headings: dust, extinction — galaxies: individual (M31) — galaxies: ISM — galaxies: photometry — H II regions

1. INTRODUCTION

Two characteristics make M31, the Andromeda galaxy, unique for a far-infrared (FIR) study. The first is its proximity: being the nearest spiral galaxy outside the Milky Way, it offers the best linear resolution for observations of spirals with a given angular resolution. This is a significant advantage for FIR observations, given the relatively poor angular resolution of the current generation of FIR instruments. Second, it is known to have a very low current star formation rate, perhaps an order of magnitude lower than that of the Milky Way (Walterbos 1988). Because of their very low FIR luminosities, not many such quiescent spirals can be studied in the FIR, and none except M31 can be studied with such high spatial resolution.

The FIR emission of M31 has been studied by Habing et al. (1984), Soifer et al. (1986), and very extensively by Walterbos & Schwering (1987, hereafter WS87) using *IRAS* maps. The main results from these early studies can be summarized as follows:

1. M31 emits only a few percent of its total luminosity at wavelengths longer than 10 μm. The rest is mainly the optical radiation from stars (Habing et al. 1984; WS87).

2. In the central part of the *IRAS* maps, corresponding to the optical bulge, the 12 and 25 μm radiation is caused by circumstellar dust emission from late-type stars, while the 60 and 100 μm emission is caused by the interstellar dust heated by the interstellar radiation field (ISRF) powered by the old bulge stars (Soifer et al. 1986).

3. The disk IR emission is strongly concentrated in a ring with a semimajor axis of ~ 45 and coincides in detail with the distribution of H II regions (Habing et al. 1984; see also Devereux et al. 1994). When it is decomposed into a warm (40 K) component associated with star formation regions and a cool component associated with "cirrus" (Cox, Krügel, & Mezger 1986; Helou 1986), less than 10% is attributable to the former (WS87).

4. The strong mid-infrared (12 and 25 μm) excess and the rather constant 60:100 μm ratio in the disk show evidence of the existence of very small grains and large molecules (WS87; Helou 1986; Xu & Helou 1994).

Recently, Devereux et al. (1994) made a comparison between the FIR emission and the Hα emission of M31 and argued that the close correspondence between the FIR and the Hα images suggests a common origin for the two emissions. According to these authors, up to 70% of the FIR emission of M31 could be associated with massive star formation regions, directly conflicting with the earlier result of WS87 (see above item 3).

We are carrying out a new FIR study on M31, utilizing the high-resolution maps (of $\sim 1'$ resolution) produced with the HiRes software (Aumann, Fowler, & Melnyk 1990; Rice 1993). Our motivation is to study the properties of FIR sources and the diffuse emission in the M31 disk *separately*. This was not possible in the earlier studies because of the relatively coarse resolution of *IRAS* maps. In an earlier paper (Xu & Helou 1994), we studied the *IRAS* color-color diagrams of a complete sample of small areas ($2' \times 2'$) in the M31 disk and found evidence for a deficiency of very small grains (but not the polycyclic aromatic hydrocrbon [PAH] molecules) in the areas dominated by the diffuse emission.

In this and a companion paper, we present a study on the general properties of FIR sources and of the diffuse emission in M31. In this paper (Paper I), we study the overall morphology of the FIR emission and the properties of the discrete sources in the M31 disk. In order to address the controversy as to the extent to which massive ionizing stars are responsible for the

FIR emission of M31 (WS87; Devereux et al. 1994), we estimate the ratio between the FIR and Hα fluxes of H II regions using those 60 μm sources which are fully covered in the Hα survey of Walterbos & Braun (1992, hereafter WB92). We present the new HiRes maps of M31 in § 2. The procedure of source extraction is described in § 3. The FIR colors of some "isolated" sources are studied in § 4. In § 5 we calculate the total dust emission of M31, from the sources and from the diffuse component, respectively, and an estimate of the present-day star formation rate of M31 is made. Section 6 contains the summary. Throughout this paper we assume for M31 a distance of 690 kpc (1′ = 200 pc along the major axis), an inclination angle of $i = 77°$ ($i = 0$ for face-on), and P.A. = 37°.

2. HIGH-RESOLUTION *IRAS* MAPS

The high-resolution *IRAS* maps of M31 at 12 μm, 25 μm, 60 μm, and 100 μm are new *IRAS* products from the Infrared Processing and Analysis Center (IPAC), using the IPAC High-Resolution (HiRes) processor (Aumann et al. 1990; Rice 1993). After the 20th iteration of the deconvolution, the resolution achieved is 0.′9 × 0.′5 (in cross-scan and in-scan directions, respectively) for the 12 and 25 μm maps, 1.′0 × 0.′8 for the 60 μm map, and 1.′5 × 1.′5 for the 100 μm map (see also Rice 1993). However, the resolution is not uniform across the maps (Fowler & Aumann 1993), and it depends in particular on the surface brightness of the background. In order to overcome this problem, and also to simplify the comparison between the four maps, we smooth all of them to a 1.′7 circular beam on a grid with 0.′5 pixels. The details of the production of the maps, and a comparison with previous M31 *IRAS* maps, can be found in Xu & Helou (1994; see also Xu & Helou 1995).

These smoothed maps are presented in Figures 1–4. Allowing for the difference in sensitivity, the four maps have similar morphology, characterized by a bright nucleus-plus-ring structures with the ring coinciding with that of the H II regions (Pellet et al. 1978 and the nucleus coinciding with the optical bulge. This has been noticed in previous studies (Habing et al. 1984; WS87). The new HiRes maps, however, reveal features with a linear scale of a few hundred parsecs to ~1 kpc, namely, the bright sources (giant star formation regions) and the very narrow widths of bright arms. Indeed, it is rather surprising that the arms are so thin that they are hardly resolved by the HiRes beams in the cross-arm direction even on the original HiRes maps (resolution of ~1′). Compared to previous results (e.g., WS87), the contrast between the arm segments (including the "ring") and the interarm region is significantly enhanced in the new HiRes maps (e.g., the 60 μm map), with a typical value of about a factor of 5 (avoiding the bright sources). Unfortunately, one cannot exclude the possibility that the contrast is artificially exaggerated by HiRes. These results will, however, be tested in the upcoming *Infrared Space Observatory* (*ISO*) mission.

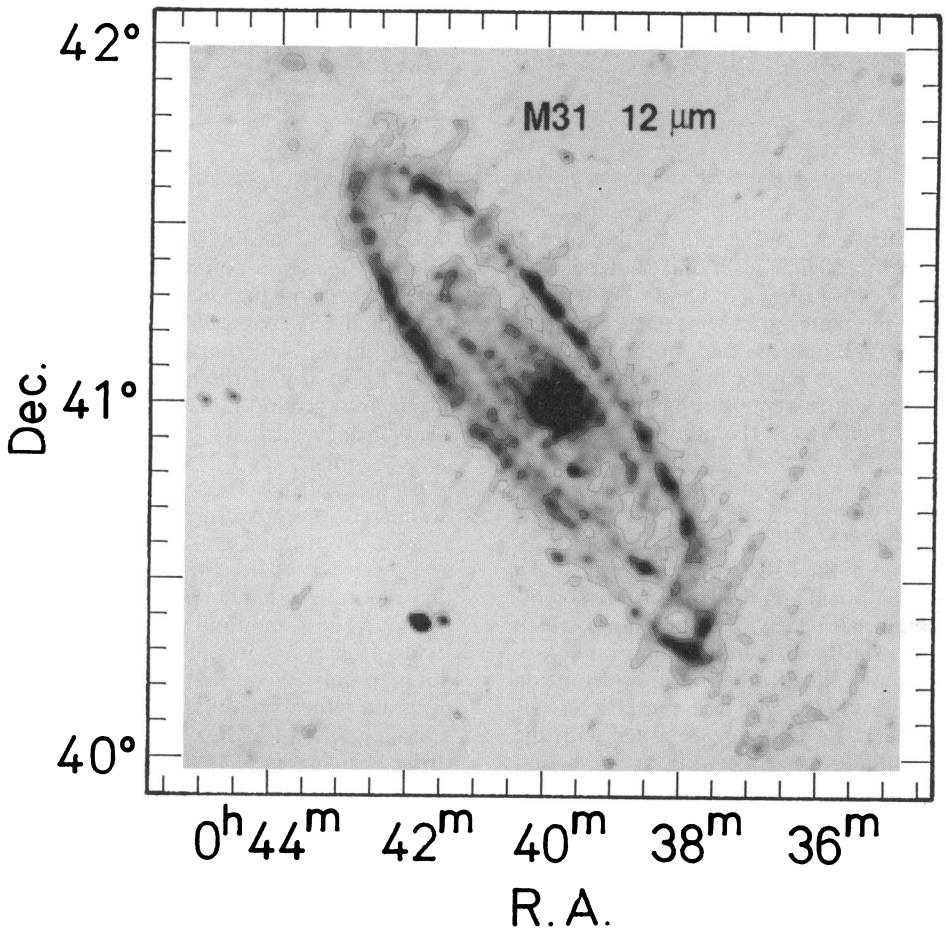

FIG. 1.—Gray-scale map (overlain with contours) of M31 at 12 μm. Beam size is 1.′7 (same as in the following maps). Contour levels are 0.3, 0.9, and 2.7 MJy sr^{-1}.

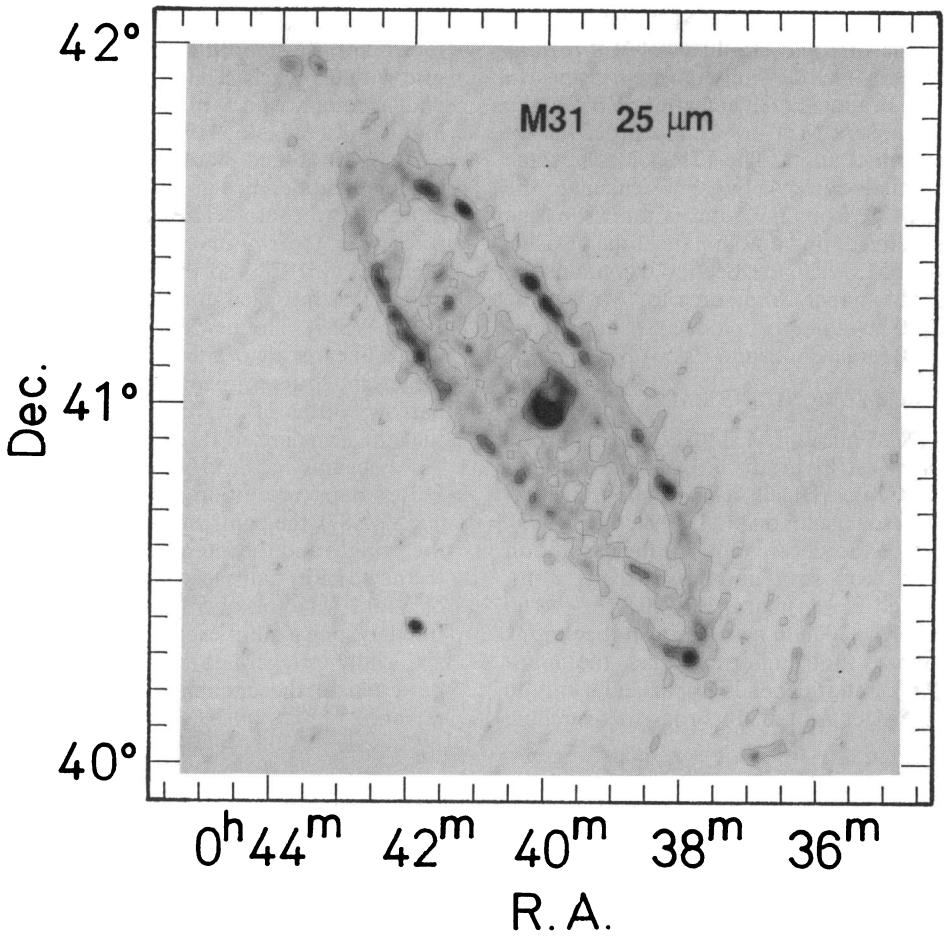

FIG. 2.—Gray-scale map (overlain with contours) of M31 at 25 μm. Contour levels are 0.3, 0.9, and 2.7 MJy sr^{-1}.

In the four panels of Figure 5, we compare the surface brightness distribution of the 60 μm map and that of a 1.7 resolution H I map (Brinks 1984; Brinks & Shane 1984) along two cuts, running through the center of M31 at position angles of 24° and of 50°, respectively. It appears that on the two maps there is good correspondence between the positions of features (dips and bumps), and the bumps representing the arm segments have about the same widths. On the other hand, the H I emission decreases toward the center of the galaxy, while the 60 μm emission does not. In comparison with optical maps of similar angular resolution (Walterbos & Kennicutt 1987), the FIR nucleus is smaller than the optical bulge, and the disk emission is much less smooth in the FIR than in the optical. An anticorrelation between the optical and the FIR surface brightness can be found in some places, e.g., the dust lanes which appear as bright thin arms on the FIR map, a natural consequence of the dust-absorbing optical radiation and reemitting in the FIR. Devereux et al. (1994) compared the HIRes FIR (40–120 μm) map with the Hα CCD image obtained with the Case Western Burrell Schmidt telescope at Kitt Peak and found "striking correspondence" between the two.

3. SOURCE EXTRACTION

There are many bright discrete sources on the HiRes maps. The brightest ones are concentrated on the famous "ring" at about 9 kpc (45′) galactocentric radius. Compared to the H II region map (Pellet et al. 1978; WB92; Devereux et al. 1994), these sources, except the nucleus, coincide exclusively with bright H II region complexes. A comparison between the 60 μm sources and the optical H II regions (WB92) reveals that individual FIR sources include typically three to five bright H II regions. The companion elliptical galaxy M32 does not show up in any of the four *IRAS* maps (Habing et al. 1984). Bright background radio sources (Berkhuijsen, Wielebinski, & Beck 1983), which do not belong to the M31 disk, are not detected either.

Because of the coarse resolution of *IRAS*, no analysis on discrete FIR sources in M31 could be carried out in previous studies. Even with the HiRes maps, many sources are still affected by confusion, in particular on the 100 μm map where they are more extended (Fig. 4) and the spatial resolution is the poorest. The 12 μm and 25 μm maps have low signal-to-noise levels. Hence, an overall source extraction is done for the 60 μm map only. We at first run an automatic source subtraction program which fits individual single elliptical Gaussians over areas of 4.5 × 4.5. For a source extraction threshold at a surface brightness of 1 MJy sr^{-1} above the background set by the local diffuse emission, we found 70 sources (excluding the nucleus) on the 60 μm map (Xu & Helou 1993). The limit was assigned because the 1 σ random fluctuation of the diffuse emission in the 60 μm disk of M31 is of the order of 0.5 MJy sr^{-1}. Therefore, the sources are reliable at $\gtrsim$95% confidence level ($\geq$2 σ level). Because of the source confusion problem, the parameters (e.g., the major axis and minor axis, the flux,

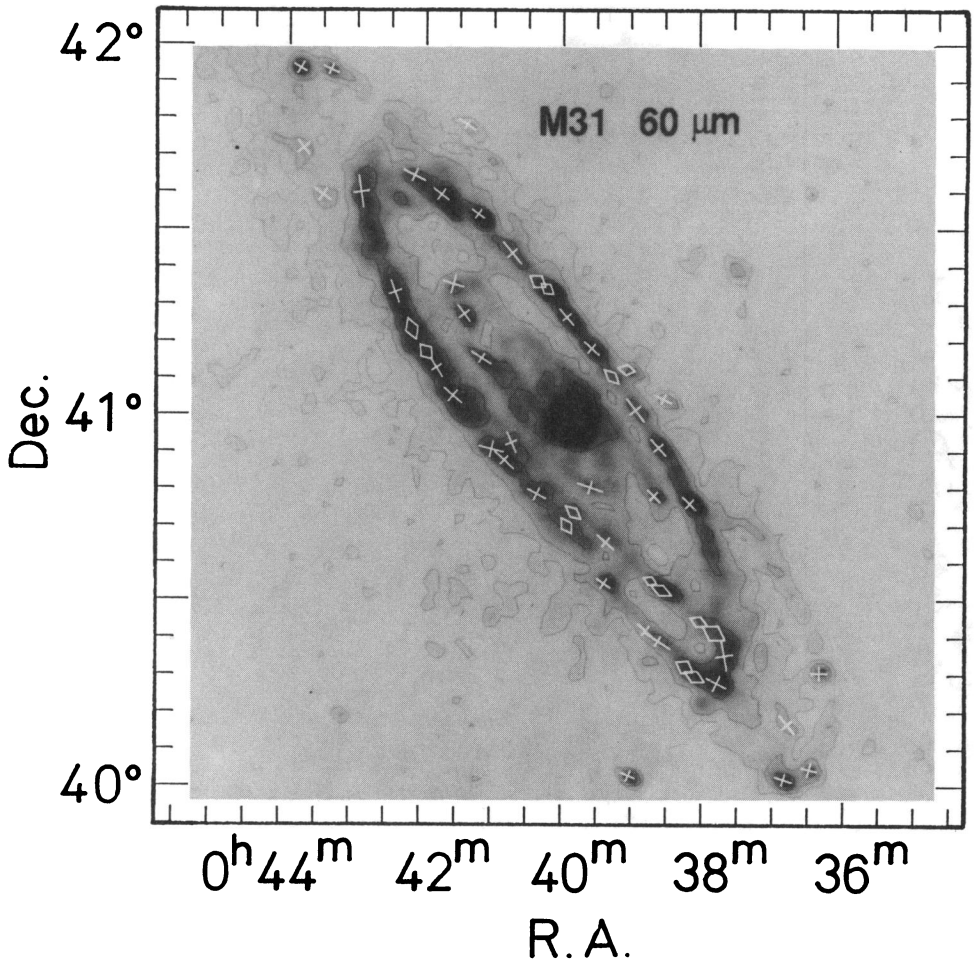

FIG. 3.—Gray-scale map (overlain with contours) of M31 at 60 μm. Contour levels are 0.3, 0.9, 2.7, and 8.1 MJy sr^{-1}. Unconfused sources (Table 1) are represented by the white crosses, each showing the location, size, and orientation of a single source. Open diamonds represent the confused sources (Table 2), each standing for a single component in a pair in Table 2.

and even the detection) for many sources vary significantly when the size of the fitting area is changed. In order to assess the uncertainty caused by this factor, we repeat the source extraction program using two more sizes of fitting area, i.e., 3′ × 3′ and 6′ × 6′. Out of the 70 sources detected in the first run (with the size of the fitting area of 4.′5 × 4.′5), 39 are detected in both these two latter runs. They are represented by crosses in Figure 3.

For each of the 39 sources we have estimated, and reported in Table 1, the values and uncertainties of the following parameters: the coordinates R.A. (1950) and decl. (1950), the peak value of the 60 μm surface brightness S_p, the major (maj) and minor (min) axes, and the position angle of the major axis P.A. (measured from the north toward the east). For any parameter x, the vlues is estimated from the weighted mean of the logarithms of corresponding results in the three different fittings:

$$\langle \ln(x) \rangle = \frac{\sum_{i=1}^{3} \omega_i \ln(x_i)}{\sum_{i=1}^{3} \omega_i}, \quad (1)$$

where x_i represents the value of the parameter found in one of the fittings, and ω_i is the weight:

$$\omega_i = \frac{1}{(\sigma_i/x_i)^2}, \quad (2)$$

where the σ_i is the uncertainty on x_i. The variance of the logarithm is estimated with the same weight, and the systematic uncertainties resulting from the different Gaussian fittings are allowed for by introducing a scaling parameter s (Eadie et al. 1977):

$$s = \frac{1}{n-1} \sum_{i=1}^{n} \left[\frac{\ln(x_i) - \langle \ln(x) \rangle}{(\sigma_i/x_i)} \right]^2 = \frac{1}{n-1} \sum_{i=1}^{n} \omega_i [\ln(x_i) - \langle \ln(x) \rangle]^2, \quad (3)$$

and

$$\sigma^2[\ln(x)] = s \frac{\sum_{i=1}^{n} \omega_i (\sigma_i/x_i)^2}{\sum_{i=1}^{n} \omega_i} = \frac{n}{n-1} \frac{\sum_{i=1}^{n} \omega_i [\ln(x_i) - \langle \ln(x) \rangle]^2}{\sum_{i=1}^{n} \omega_i}, \quad (4)$$

with $n = 3$. The values and uncertainties listed in Table 1 are calculated from these means and variances:

$$x = e^{\langle \ln(x) \rangle} \quad (5)$$

$$\sigma(x) = x \sqrt{\sigma^2[\ln(x)]}. \quad (6)$$

The uncertainties of the peak surface brightness and of the total flux of each source include also the calibration uncer-

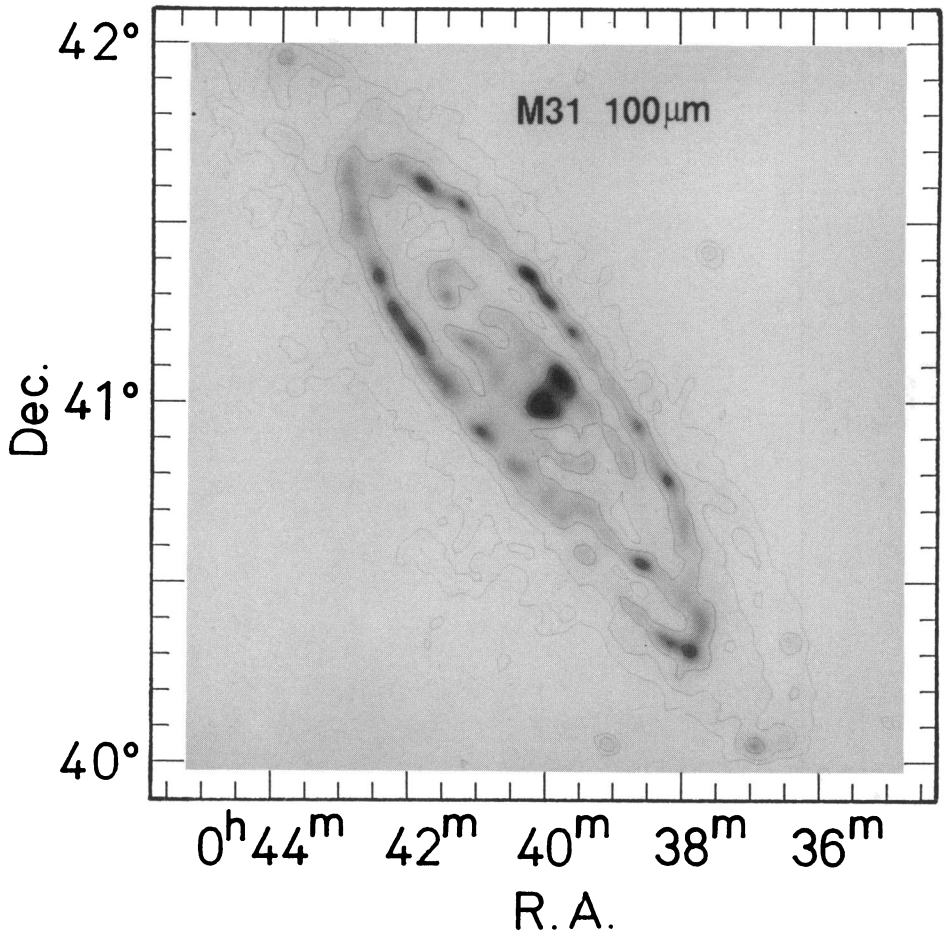

FIG. 4.—Gray-scale map (overlain with contours) of M31 at 100 μm. Contour levels are 1.2, 3.6, and 10.8 MJy sr^{-1}.

tainty of the 60 μm map, which is at 4% level (Xu & Helou 1994).

The columns of Table 1 are arranged as follows (uncertainty of each value follows in parentheses):

Column (1): source identification in the list.
Column (2): The 1950 equinox right ascension (R.A.) in hours, minutes, and seconds.
Column (3): The 1950 equinox declination (decl.) in degrees, arcminutes, and arcseconds.
Column (4): Peak 60 μm surface brightness S_p in MJy sr^{-1}.
Column (5): Major axis of the source in arcminutes.
Column (6): Minor axis of the source in arcminutes.
Column (7): Position angle of the major axis in degrees.
Column (8): 60 μm flux in Jy.
Column (9): Sum of the Hα fluxes of the corresponding H II regions in 10^{-12} ergs cm^{-2} s^{-1}, taken from WB92.
Column (10): Identification of the corresponding H II regions in the catalog of WB92 for ionized nebulae in the northeast half of M31.

In addition, another 14 confused sources form seven pairs (Table 2). For each pair, two sources are detected individually in the test run with the fitting area size of 3′ as well as in the original run with the fitting area size of 4.′5, but in the run with the fitting size of 6′ the two components are not distinguished, and therefore only one large source is detected. These confused sources are marked by open diamonds on the 60 μm map (Fig. 3) and listed in Table 2. The combined flux $f_{60\,\mu m}$ and its uncertainty is calculated for each pair using the similar formulae as given in equations (1)–(6) with $f_{60\,\mu m,1} = f^{a}_{60\,\mu m,1} + f^{b}_{60\,\mu m,1}$ and $f_{60\,\mu m,2} = f^{a}_{60\,\mu m,2} + f^{b}_{60\,\mu m,2}$, where subscripts 1 and 2 denote the values found in the Gaussian fittings with areas 3′ × 3′ and 4.′5 × 4.′5, respectively, and superscripts a and b represent the values for components a and b. The flux $f_{60\,\mu m,3}$ is taken from that of the single source (including both components) found in Gaussian fitting to the 6′ × 6′ area. The $f_{60\,\mu m}$ of source pair 4a + 4b has a large uncertainty (78%) owing to the large dispersion among the three fittings (the factor s in eq. [3] is large). Because of the confusion problem, for individual components of each pair we list only the right ascension and declination which are calculated from the weighted mean of the corresponding values found in the two Gaussian fittings using areas of 3′ × 3′ and 4.′5 × 4.′5, respectively.

4. *IRAS* COLORS OF ISOLATED SOURCES

From Table 1 we selected 10 bright ($f_{60\,\mu m} > 1$ Jy) "isolated" sources (Table 3) around which there are no other sources within twice the Gaussian radius. Therefore, they do not suffer the confusion problem seriously. The *IRAS* colors of these isolated sources will be studied in this section, which are presumably representative for the discrete sources in general.

At the position of each isolated 60 μm source, we did source extractions on the other three maps (i.e., the 12 μm map, 25 μm

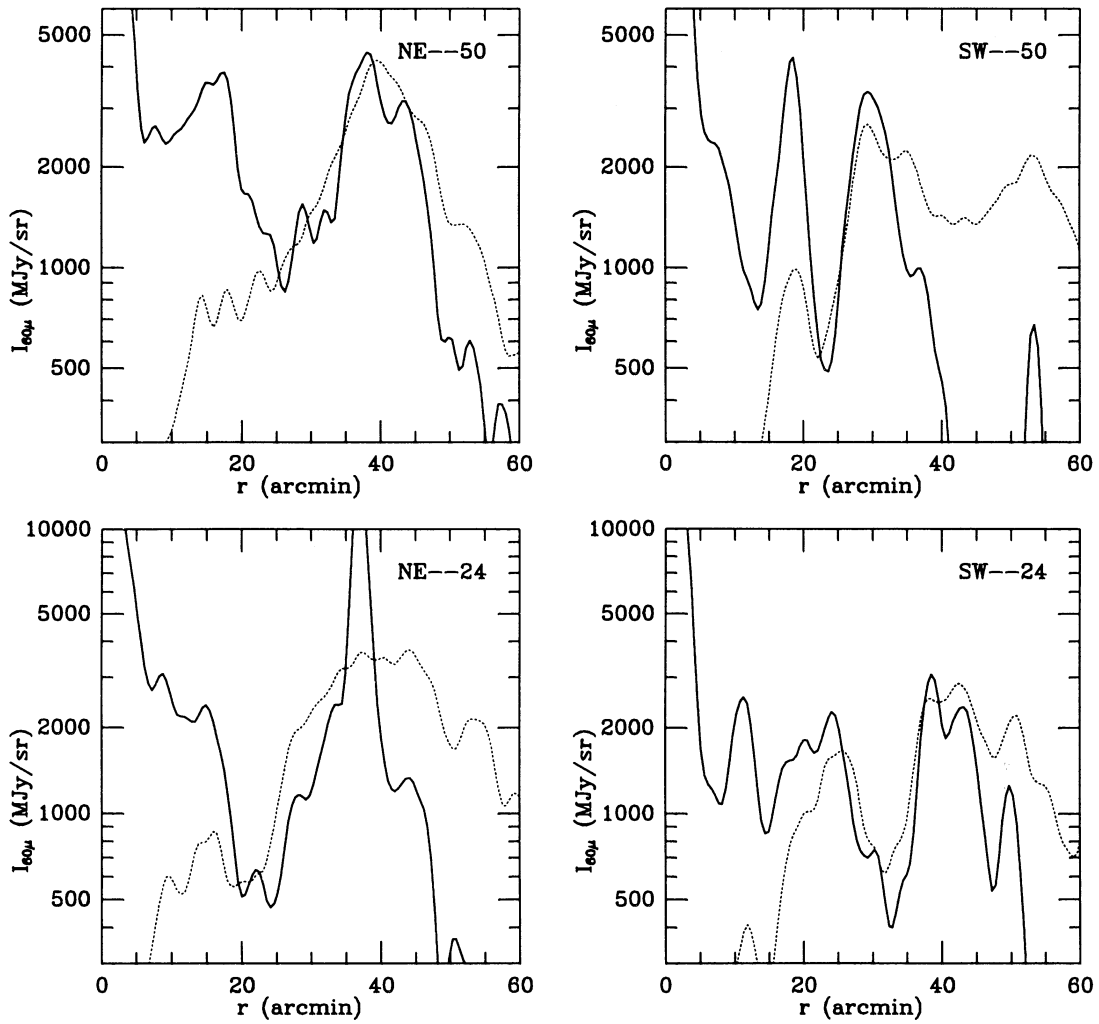

FIG. 5.—Comparison between the 60 μm surface brightness distribution (*solid curve*) and the H I column density distribution (*dotted curve*) along two cuts both passing through the center of M31. The H I column density is plotted with arbitrary units. (*Top left*) Along the cut with the position angle P.A. = 50°, in the northeast half of M31. (*Top right*) Along the same cut, in the southwest half of M31. (*Bottom left*) Along the cut with the position angle P.A. = 24°, in the northeast half of M31. (*Bottom right*) Along the same cut, in the southwest half of M31.

map, and the 100 μm map) using single elliptical Gaussian fittings. For each source and each map, the source extraction is repeated three times, with the size of the fitting area equal to 3′ × 3′, 4.′5 × 4.′5, and 6′ × 6′, respectively. All sources are detected in each of the three maps at least in two of the three runs with different areas. In Table 3 we give their fluxes and the uncertainties in the *IRAS* bands, calculated using similar formulae to those given in equations (1)–(6). Some sources were detected only in two of the three Gaussian fittings (again with the size of the fitting area equal to 3′ × 3′, 4.′5 × 4.′5, and 6′ × 6′, respectively) at wavelengths other than 60 μm. In these cases, the corresponding flux and the uncertainty are calculated from the results in the two successful fittings and are followed by a colon. The uncertainties include the calibration uncertainties of the corresponding maps, which are at 11%, 9%, 4%, and 10% levels for the 12 μm, 25 μm, 60 μm, and 100 μm maps, respectively (Xu & Helou 1994).

The columns of Table 3 are arranged as follows (uncertainty of each value follows in parentheses):

Column (1): Source identification in Table 1.
Column (2): 12 μm flux $f_{12\ \mu m}$ in Jy.
Column (3): 25 μm flux $f_{25\ \mu m}$ in Jy.
Column (4): 60 μm flux $f_{60\ \mu m}$ in Jy.
Column (5): 100 μm flux $f_{100\ \mu m}$ in Jy.

Figure 6 is an *IRAS* color-color diagram [log $(f_{12\ \mu m}/f_{25\ \mu m})$ vs. log $(f_{60\ \mu m}/f_{100\ \mu m})$] of these isolated sources which shows a clear anticorrelation between the colors. This anticorrelation has been found for galaxies (Helou 1986), for regions surrounding very massive stars (Boulanger et al. 1988), and for a complete sample of small areas within the M31 disk (Xu & Helou 1994). The trend found by WS87 that regions of high 60 μm to 100 μm intensity ratio correspond to relative depressions in the 12 μm to 100 μm intensity ratio may also be of the same nature (Helou, Ryter, & Soifer 1991).

The FIR color ratio $(f_{60\ \mu m}/f_{100\ \mu m})$ of the sources varies in the range from ~0.2, which is slightly higher than the color ratio of the diffuse emission (0.17; see Xu & Helou 1994), to 0.5, with a mean of 0.30 ± 0.04. The means of other two *IRAS* colors are $\langle f_{12\ \mu m}/f_{60\ \mu m}\rangle = 0.14 \pm 0.02$ and $\langle f_{25\ \mu m}/f_{60\ \mu m}\rangle = 0.19 \pm 0.02$.

The mean $\langle f_{60\ \mu m}/f_{100\ \mu m}\rangle = 0.30 \pm 0.04$ corresponds to a color temperature of 26 ± 1 K (ν^2 emissivity law). Cox &

1996ApJ...456..152X

TABLE 1

LIST OF DISCRETE 60 μm SOURCES

Identification (1)	R.A. (1950) (2)	Decl. (1950) (3)	S_p (MJy sr^{-1}) (4)	Major Axis (5)	Minor Axis (6)	P.A. (7)	$f_{60\,\mu m}$ (Jy) (8)	f(Hα) (10^{-12} ergs cm^{-2} s^{-1}) (9)	H II Regions (10)
1	00^{h}36^{m}59^s.0 (0.1 s)	40°04′05″.5 (0″.8)	6.30 (0.26)	2′.77 (0.10)	1′.83 (0′.03)	70°.7 (1°.5)	3.06 (0.18)	...	...
2	00 39 09.1 (0.0)	40 04 44.9 (0.3)	5.96 (0.24)	2.27 (0.04)	1.60 (0.01)	66.4 (0.9)	2.08 (0.09)	...	...
3	00 36 37.3 (0.2)	40 05 37.3 (0.3)	3.08 (0.13)	2.38 (0.10)	2.18 (0.14)	74.3 (5.2)	1.53 (0.13)	...	...
4	00 36 55.6 (1.1)	40 12 41.9 (10.5)	1.00 (0.06)	3.68 (0.24)	1.92 (0.12)	39.2 (4.4)	0.68 (0.08)	...	...
5	00 37 54.8 (0.6)	40 19 14.7 (5.7)	6.76 (0.34)	3.42 (0.24)	2.60 (0.11)	62.7 (3.2)	5.76 (0.55)	...	...
6	00 36 27.9 (0.1)	40 20 47.4 (1.1)	3.42 (0.14)	2.42 (0.05)	1.97 (0.04)	89.3 (0.7)	1.57 (0.08)	...	...
7	00 37 48.0 (0.1)	40 23 29.5 (7.2)	4.10 (0.31)	4.47 (0.65)	2.70 (0.21)	9.8 (4.5)	4.73 (0.86)	...	...
8	00 38 43.6 (0.7)	40 25 50.7 (6.1)	2.31 (0.18)	4.64 (0.73)	1.60 (0.05)	57.3 (1.9)	1.64 (0.29)	...	...
9	00 38 54.2 (0.6)	40 27 25.5 (6.8)	1.30 (0.13)	2.99 (0.59)	1.78 (0.11)	48.2 (2.9)	0.66 (0.22)	...	...
10	00 39 29.4 (0.2)	40 34 47.4 (1.8)	4.47 (0.20)	2.53 (0.16)	1.73 (0.05)	55.6 (2.7)	1.88 (0.16)	...	...
11	00 39 27.5 (6.3)	40 41 13.0 (4.9)	1.38 (0.13)	3.45 (0.51)	1.75 (0.10)	48.3 (2.1)	0.80 (0.14)	...	...
12	00 38 16.7 (0.0)	40 47 12.1 (0.4)	11.05 (0.46)	2.88 (0.25)	1.79 (0.03)	44.7 (1.3)	5.46 (0.54)	...	...
13	00 40 26.0 (0.2)	40 48 48.5 (1.5)	2.86 (0.25)	3.21 (0.32)	2.07 (0.19)	61.9 (2.1)	1.83 (0.30)	...	...[a]
14	00 38 46″.6 (0.0)	40 48 23.1 (2.8)	3.79 (0.19)	2.70 (0.30)	1.71 (0.06)	46.3 (2.1)	1.68 (0.21)	...	...
15	00 39 40.5 (1.3)	40 49 44.0 (0.3)	1.76 (0.10)	4.09 (0.66)	1.87 (0.13)	71.9 (2.4)	1.29 (0.24)	...	...
16	00 40 53.6 (0.9)	40 54 03.0 (9.9)	5.40 (0.51)	4.06 (0.45)	1.67 (0.09)	47.2 (1.3)	3.50 (0.54)	3.33 (0.10)	160,172,189
17	00 41 04.6 (0.6)	40 55 48..0 (8.9)	3.72 (0.58)	3.86 (0.20)	2.47 (0.13)	75.7 (3.6)	3.40 (0.60)	1.81 (0.03)	206,207,245
18	00 38 42.5 (0.4)	40 55 57.4 (6.2)	5.82 (0.31)	3.47 (0.22)	1.78 (0.04)	41.8 (0.9)	3.45 (0.29)	...	...
19	00 40 47.5 (1.1)	40 56 47.6 (24.7)	1.31 (0.12)	3.48 (0.43)	1.83 (0.13)	23.7 (7.2)	0.80 (0.14)	...	...[b]
20	00 39 02.1 (0.6)	41 01 51.9 (10.0)	2.83 (0.18)	4.46 (0.86)	2.15 (0.10)	37.3 (1.6)	2.60 (0.54)	...	...
21	00 38 38.1 (0.3)	41 03 34.0 (3.2)	1.89 (0.09)	2.82 (0.09)	1.51 (0.05)	62.9 (1.6)	0.77 (0.05)	...	...
22	00 41 37.3 (0.0)	41 04 13.8 (1.5)	6.15 (0.37)	3.63 (0.51)	2.13 (0.14)	49.1 (4.9)	4.56 (0.75)	4.37 (0.17)	403,410,414
23	00 41 51.4 (0.2)	41 08 39.4 (7.6)	7.65 (0.39)	3.47 (0.64)	1.78 (0.08)	32.3 (1.7)	4.53 (0.88)	2.23 (0.05)	458,490,501
24	00 41 13.0 (0.2)	41 10 07.2 (1.8)	4.68 (0.22)	3.59 (0.60)	1.59 (0.04)	56.7 (1.7)	2.55 (0.45)	...	...[c]
25	00 39 39.0 (0.3)	41 11 36.9 (3.0)	7.79 (0.36)	3.08 (0.30)	1.72 (0.05)	48.8 (1.5)	3.96 (0.43)	0.77 (0.03)	25,36,39
26	00 40 00.2 (0.4)	41 16 31.1 (5.3)	10.41 (0.53)	3.33 (0.30)	1.64 (0.05)	41.3 (1.2)	5.45 (0.57)	...	...[d]
27	00 41 27.9 (0.1)	41 17 02.5 (0.8)	4.65 (0.20)	3.09 (0.21)	1.88 (0.04)	37.7 (1.0)	2.58 (0.22)	1.83 (0.07)	305,314,315
28	00 42 26.9 (0.1)	41 20 30.0 (4.5)	9.38 (0.41)	3.56 (0.31)	2.05 (0.07)	20.7 (1.4)	6.55 (0.65)	3.51 (0.14)	695,703,722
29	00 41 37.0 (0.8)	41 21 40.3 (1.7)	2.25 (0.11)	3.26 (0.43)	2.76 (0.15)	74.1 (6.8)	1.94 (0.29)	...	...[e]
30	00 40 46.8 (2.2)	41 26 27.1 (26.2)	2.35 (0.14)	4.40 (0.64)	1.86 (0.09)	39.9 (5.1)	1.84 (0.30)	0.69 (0.02)	132,139,148,154
31	00 41 15.9 (0.1)	41 32 32.7 (0.3)	18.04 (0.74)	2.31 (0.07)	1.63 (0.02)	53.6 (0.8)	6.52 (0.34)	2.08 (0.08)	243,267,280
32	00 43 29.2 (0.3)	41 35 35.6 (2.4)	1.22 (0.06)	3.03 (0.15)	2.24 (0.09)	54.6 (2.1)	0.80 (0.07)	...	...[f]
33	00 41 47.6 (0.2)	41 35 35.6 (2.0)	12.63 (0.51)	2.92 (0.28)	2.01 (0.04)	52.7 (2.1)	7.12 (0.72)	3.58 (0.14)	442,453,496
34	00 42 56.2 (0.6)	41 36 02.0 (3.9)	4.08 (0.21)	4.78 (0.91)	2.46 (0.12)	8.3 (2.0)	4.60 (0.93)	...	...[g]
35	00 42 10.4 (0.7)	41 38 33.0 (6.5)	3.33 (0.17)	3.74 (0.30)	1.90 (0.07)	63.8 (4.1)	2.27 (0.23)	1.12 (0.04)	589,599,631,653
36	00 43 45.9 (0.8)	41 42 51.3 (3.0)	1.28 (0.06)	2.72 (0.46)	2.25 (0.27)	37.7 (4.1)	0.76 (0.17)	...	...[h]
37	00 41 25.8 (0.0)	41 46 20.1 (1.5)	1.18 (0.05)	3.12 (0.27)	1.46 (0.05)	56.6 (1.3)	0.52 (0.06)	...	...
38	00 43 22.5 (0.1)	41 55 04.4 (0.9)	3.96 (0.17)	2.52 (0.22)	1.65 (0.03)	64.9 (1.0)	1.58 (0.15)	...	...[i]
39	00 43 48.8 (0.1)	41 55 23.3 (0.7)	6.64 (0.27)	2.23 (0.07)	1.98 (0.04)	58.4 (2.9)	2.81 (0.15)	2.33 (0.08)	922,927,932

[a] In the northeast part of the M31 disk but outside the southwest boundary of Plate 2 of WB92.
[b] In the northeast part of the M31 disk but outside the north boundary of Plate 2 and the west boundary of Plate 3 of WB92.
[c] In the northeast part of the M31 disk but outside the northwest boundary of Plate 4 of WB92.
[d] In the northeast part of the M31 disk but outside the southwest boundary of Plate 15 of WB92.
[e] In the northeast part of the M31 disk but partially outside the north boundary of Plate 1 of WB92.
[f] In the northeast part of the M31 disk but outside the southeast boundary of Plate 10 of WB92.
[g] In the northwest part of the M31 disk but outside the south boundary of Plate 10 of WB92.
[h] In the northwest part of the M31 disk but outside the east boundary of Plate 10 of WB92.
[i] In the northeast part of the M31 disk but partially outside the east boundary of Plate 19 of WB92.

TABLE 2

LIST OF CONFUSED 60 μm SOURCES (SOURCE PAIRS)

Identification (1)	R.A. (1950) (2)	Decl. (1950) (3)	$f_{60\,\mu m}$[a] (Jy) (4)
1a	00h38m13s.0	40°20′15″.2	4.43 (0.34)
1b	00 38 21.4	40 21 47.6	
2a	00 37 56.7	40 27 04.4	2.89 (1.32)
2b	00 38 09.4	40 28 49.0	
3a	00 38 40.8	40 33 42.8	5.28 (0.79)
3b	00 38 50.1	40 35 10.0	
4a	00 40 00.8	40 43 47.4	2.76 (2.15)
4b	00 39 54.8	40 45 50.9	
5a	00 39 22.0	41 07 09.9	2.51 (1.13)
5b	00 39 09.4	41 08 16.2	
6a	00 41 60.0	41 11 07.1	9.27 (1.92)
6b	00 42 12.4	41 14 42.3	
7a	00 40 16.9	41 20 53.6	9.65 (0.90)
7b	00 40 24.9	41 21 57.5	

[a] Combined flux for each pair of confused sources. Uncertainty listed in parentheses.

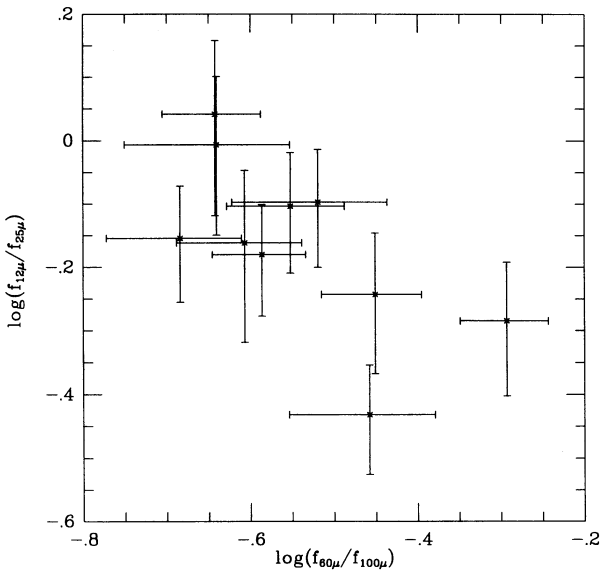

FIG. 6.—$R(60, 100) = f_{60\,\mu m}/f_{100\,\mu m}$ vs. $R(12, 25) = f_{12\,\mu m}/f_{25\,\mu m}$ diagram of 10 isolated sources (see the text).

Mezger (1988) and Rice et al. (1990) also found that for sources in the Galaxy and in M33 the average color temperature is about 30 K, rather than 40 K, as assumed in WS87 and in other early papers (e.g., Cox et al. 1986). On the other hand, it appears that on average M31 sources are probably cooler than the M33 sources which have a mean $f_{60\,\mu m}/f_{100\,\mu m} = 0.40 \pm 0.11$ (Rice et al. 1990), although the difference is not significant because of the large error bars. This possible difference would be consistent with the optical studies of M31 H II regions which show (1) the lack of bright regions and a possible excess of faint regions compared to other nearby spiral galaxies (Kennicutt, Edgar, & Hodge 1989; WB92), and (2) the giant H II regions in M31 being more diffuse than those in the Galaxy and in M33 (Kennicutt 1984). It might also be caused by the deficiency of the very small grains in the M31 disk (Xu & Helou 1994).

5. LUMINOSITY OF THE H II REGION–ASSOCIATED FIR COMPONENT AND THE PRESENT-DAY STAR FORMATION RATE

The FIR sources in M31 coincide generally with giant H II regions or H II complexes. This agrees fully with the results in the literature. Cox & Mezger (1988) and Pérault et al. (1989) used the longitudinal profiles of Galactic emission in *IRAS* bands to separate the FIR sources and the diffuse emission in the Galaxy and found that all the sources are associated with bright Giant Molecular Clouds/H II complexes, spiral arm segments, and the Galactic center. Rice et al. (1990) detected 19 sources in the *IRAS* maps of M33 (3′ × 5′ resolution), all coincident with H II regions cataloged at optical and radio wavelengths. For the Large Magellanic Cloud, with *IRAS* maps of resolution of ~3′ × 3′, Xu et al. (1992) found that the probability of coincidence between bright FIR sources and bright H II regions is better than 90%. On the other hand, it is very likely that some H II regions which are faint and do not cluster around any giant H II regions will not appear as bright FIR sources, namely, that part of the H II region–associated FIR emission may not be represented by the FIR sources.

We try to estimate quantitatively how much the H II region–associated component contributes to the total 60 μm emission of M31, through a comparison between the 60 μm sources and the H II regions detected in the CCD Hα observations of WB92 for some regions in the northeast part of M31. The idea is that such a comparison will yield a mean of the $f_{60\,\mu m}$/Hα ratio for H II regions. Multiplying this ratio with the total Hα flux of M31 H II regions, an estimate of the total 60 μm flux of the H II region–associated component can be made. Of the sources presented in Table 1, we find 12 cases which fall in the region covered by the Hα observations. For these 12, we show the sum of the Hα fluxes (uncorrected for internal extinction) of H II regions located within the region (defined by the major and minor axes and the P.A.) of the corresponding 60 μm source. Since the resolution of the Hα observations is much higher than that of our *IRAS* maps, an FIR source usually encloses many H II regions, of which we list only the brightest few. A weighted mean (weight = $1/\sigma^2$) of $\langle f_{60\,\mu m}/f(\mathrm{H}\alpha)\rangle = 1.5(\pm 0.2)\ 10^{12}$ Jy/(ergs cm^{-2} s^{-1}) is found for these sources.

It should be pointed out that some of the diffuse Hα emission which is not cataloged as extended structures in WB92, is not included in the above calculation, so that the Hα fluxes may be underestimated and the ratio overestimated. According to Walterbos & Braun (1994), the diffuse emission contributes

TABLE 3

IRAS FLUXES OF ISOLATED SOURCES

Identification (1)	$f_{12\,\mu m}$ (Jy) (2)	$f_{25\,\mu m}$ (Jy) (3)	$f_{60\,\mu m}$ (Jy) (4)	$f_{100\,\mu m}$ (Jy) (5)
1	0.51 (0.14)	0.47 (0.07)	3.06 (0.18)	13.43 (1.62)
2	0.11: (0.01:)	0.21: (0.04:)	2.08 (0.09)	4.08 (0.46)
3	0.35 (0.04)	0.44: (0.07:)	1.53 (0.13)	5.46 (0.70)
6	0.21:0.04:	0.36 (0.07)	1.57 (0.08)	4.43 (0.56)
10	0.30 (0.04)	0.43 (0.07)	1.88 (0.16)	9.08 (1.48)
12	1.12 (0.24)	1.13 (0.18)	5.46 (0.54)	23.86 (4.81)
27	0.28 (0.08)	0.40: (0.04:)	2.58 (0.22)	10.44 (1.55)
31	0.30: (0.05:)	0.82 (0.09)	6.52 (0.34)	18.71 (3.59)
38	0.27 (0.04)	0.34 (0.05)	1.58 (0.15)	5.22 (0.98)
39	0.32: (0.05:)	0.49 (0.06)	2.81 (0.15)	10.84 (1.26)

40% of the total Hα emission of M31, some of which is included in the H II region catalog as extended structures and is therefore not missed by our estimate. On the other hand, the Hα emission associated with the 60 μm sources is clearly dominated by a few very bright discrete H II regions. Therefore, we conclude that the error resulting from the omission of some diffuse Hα emission cannot be very significant. There are nine more 60 μm sources in Table 1 in the northeast half of M31. As noted in Table 1, they are either completely or partially outside the Hα survey.

Walterbos & Braun (1994), extrapolating from their survey over the northeast part of M31, estimate that a total Hα luminosity of 1.2×10^{40} ergs s^{-1} (uncorrected for internal extinction) is radiated from the star formation regions in M31. This includes the flux from the diffuse ionized gas (DIZ) found near the regions of star formation which is likely to be photoionized by massive stars (Walterbos & Braun 1994) but which excludes the nucleus and the diffuse component in the inner part of the M31 disk, which appears not associated with star formation regions (Devereux et al. 1994). Devereux et al. (1994) find a higher Hα luminosity: excluding the nuclear emission and the diffuse emission in the inner disk, a total Hα luminosity of $1.8 \pm 0.5 \times 10^{40}$ ergs s^{-1} (uncorrected for internal extinction) is observed from the "star formation ring" in the M31 disk. However, this latter luminosity includes the emission from [N II] lines. Using the spectral data of eight Sab–Sbc galaxies in Kennicutt (1992), we find a mean Hα/(Hα + [N II]) flux ratio of 0.61 ± 0.13. Hence, the result of Devereux et al. (1994) implies a total "pure" Hα luminosity of $1.1 \pm 0.3 \times 10^{40}$ ergs s^{-1} radiated from M31 star formation regions, consistent with the estimate of Walterbos & Braun (1994). In the following, we will use this value as the estimate of the total Hα flux from M31 star formation regions.

At the adopted distance of 690 kpc, the Hα luminosity of 1.1×10^{40} ergs s^{-1} corresponds to a flux of 1.9×10^{-10} ergs cm^{-2} s^{-1}. Multiplying this Hα flux with the mean $\langle f_{60\,\mu m}/f(\mathrm{H}\alpha)\rangle$ ratio found for the 60 μm sources, we estimate that a 60 μm flux of 289 Jy, with a relative uncertainty of ~40% (including both the error of the Hα luminosity and that of the $\langle f_{60\,\mu m}/f(\mathrm{H}\alpha)\rangle$ ratio), is caused by dust associated with H II regions. This is 49% ± 19% of the total 60 μm flux of M31, and twice the sum of $f_{60\,\mu m}$ of all sources listed in Tables 1 and 2. Using this result and assuming that the mean *IRAS* colors of the isolated sources found in § 4 represent those of the H II region–associated component in general, we estimate the fluxes of the H II region–associated dust in the other three *IRAS* bands which, together with $f_{60\,\mu m}$, are presented in Table 4.

From the *IRAS* fluxes listed in Table 4, and applying the formula of Helou et al. (1988), we find that the H II region–associated component contributes $2.17(\pm 0.87) \times 10^{-8}$ ergs cm^{-2} s^{-1} of the integrated flux in the wavelength range 40–120 μm, namely, 37% ± 15% of the total flux in this wavelength range radiated from M31 (Table 4). In order to estimate its contribution to the total dust emission (8–1000 μm), we need to extrapolate both the H II region–associated component and the diffuse component to longer wavelengths beyond 120 μm. Assuming that the very small grains are only half as abundant in M31 cirrus as they are in Galactic cirrus (Xu & Helou 1994) and applying a model based on that of Désert, Boulanger, & Puget (1990) with the ISRF intensity equal to that in the solar neighborhood (Fig. 7), we find that the total dust emission for the diffuse component is $1.13(\pm 0.32) \times 10^{-7}$ ergs cm^{-2} s^{-1}, 3.1 times that of its integrated flux in the wavelength range 40–120 μm. The average spectrum of M31 sources is extended to the same wavelength range (Fig. 7) by using another model based on that of Désert et al. for IR emission near an O5 star with the dilution factor $X_{O5} = 0.003$ (i.e., dust heated at 18 pc away from the star), and with the assumption that both the very small grains and the PAHs are only half as abundant in dust associated with M31 H II regions as they are in Galactic cirrus (PAHs may be destroyed in H II regions; Boulanger et

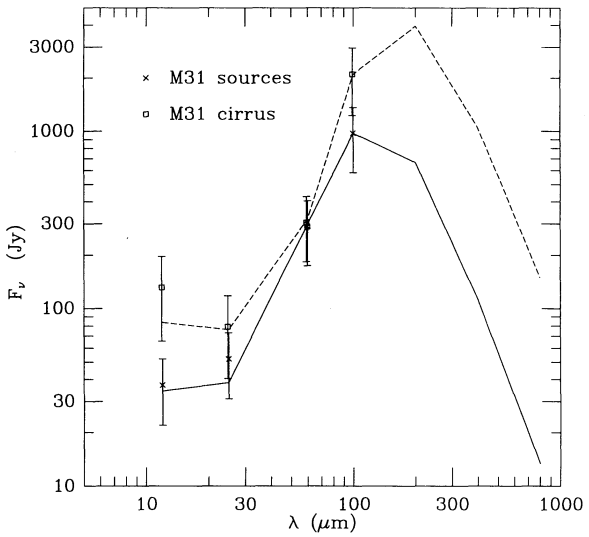

FIG. 7.—The IR spectra of M31 sources and of the diffuse component. The solid line is the spectrum calculated using a model based on that of Désert et al. (1990) for the IR emission near an O5 star with the dilution factor $X_{O5} = 0.003$, and assuming both very small grains (VSGs) and PAHs are only half as abundant as they are in Galactic cirrus. The dashed line is to extrapolate the spectrum of the diffuse component to the whole IR wavelength range using a model based on that of Désert et al. (1990) for cirrus with the intensity of the IRSF equal to that in the solar neighborhood, and assuming that the VSGs are only half as abundant as they are in Galactic cirrus.

TABLE 4

IR FLUXES AND LUMINOSITIES OF H II REGION–ASSOCIATED COMPONENT AND OF DIFFUSE COMPONENT

Component	$f_{12\,\mu m}$ (Jy)	$f_{25\,\mu m}$ (Jy)	$f_{60\,\mu m}$ (Jy)	$f_{100\,\mu m}$ (Jy)	FIR Flux[a] (10^{-8} ergs cm^{-2} s^{-1})	L_{IR}[b] (10^9 $L_\odot$)
H II	37 ± 15	52 ± 21	289 ± 115	974 ± 390	2.17 ± 0.87	0.72 ± 0.29
diffuse[c].....	131 ± 51	79 ± 42	306 ± 118	2099 ± 502	3.64 ± 0.96	1.70 ± 0.48
total[d].....	168 ± 49	131 ± 36	595 ± 28	3073 ± 316	5.81 ± 0.40	2.42 ± 0.56

[a] Integrated FIR flux between 40–120 μm.
[b] Integrated IR luminosity between 8–1000 μm.
[c] Including the nucleus.
[d] *IRAS* fluxes are different from Xu & Helou 1994. See the erratum (Xu & Helou 1995).

al. 1988). Then we find that the total dust emission of the H II region–associated component is $4.8(\pm 1.9) \times 10^{-8}$ ergs cm^{-2} s^{-1}, 2.2 times that of its integrated flux in the wavelength range 40–120 μm. In terms of luminosity in the wavelength range of 8–1000 μm, we conclude that M31 radiates $2.42(\pm 0.56) \times 10^9\ L_\odot$, of which $7.2(\pm 2.9) \times 10^8\ L_\odot$ (i.e., 30% ± 14%) is caused by the H II region–associated component (Table 4).

It is interesting to note that the total IR emission of M31 found here is very close to the result of WS87, who found a total IR emission of $2.6 \times 10^9\ L_\odot$. WS87 used a simpler two-component model with the warm component being a modified blackbody (assuming a ν^2 dust emissivity law) specified by a single temperature of 40 K, and the cool component a fixed spectrum with the $I_{60\,\mu m}/I_{100\,\mu m} = 0.16$ ($T_d = 21$ K). On the other hand, the total IR luminosity of the H II region–associated component is a factor 3.6 times the luminosity of the warm component of WS87, which is $2 \times 10^8\ L_\odot$. The low luminosity of the warm component of WS87 is likely to be a consequence of the high color temperature (40 K corresponding to $f_{60\,\mu m}/f_{100\,\mu m} \simeq 1$) adopted for the warm dust.

From the total luminosity of the H II region–associated component, we can estimate the present-day star formation rate of M31 using the formula given in Walterbos (1988): $R_{IR} = 1 \times 10^{-3} L_{IR}(\text{H II})/t_{IR}$, where R_{IR} is the star formation rate in $M_\odot$ yr^{-1}, L_{IR}(H II) is the total luminosity of the H II region–associated component, and t_{IR} is the timescale over which massive stars contribute to the heating of H II region–associated dust. Assuming $t_{IR} = 2 \times 10^6$ yr (Thronson & Telesko 1986), we find a present-day star formation rate of $R_{IR} = 0.36(\pm 0.14)\ M_\odot$ yr^{-1}, well in the range of 0.2–0.5 $M_\odot$ yr^{-1} found by Walterbos (1988) using several star formation indicators. This is about an order of magnitude lower than the present-day star formation rate of the Milky Way (Mezger 1988).

Our results show that, despite such a low present-day star formation rate, a substantial part (~30%–40%) of the FIR emission of M31 is attributable to the young high-mass ionizing stars also responsible for the H II regions. For the Milky Way, the contribution from the H II region–associated component to the total FIR emission is only 20%–30% (Cox & Mezger 1988; Pérault et al. 1989; Bloemen, Duel, & Thaddeus 1990). The relatively high contribution from the H II region–associated component to the FIR emission of M31 is probably the result of a depression of the diffuse FIR emission of interstellar dust not associated with H II regions, which in turn is caused by (1) a deficiency of the nonionizing UV radiation which is responsible for most of the heating of diffuse dust in an average spiral galaxy (Xu 1990), given that the 2000 Å–to–blue flux ratio of M31 is one of the lowest in a large sample of nearby galaxies (Buat & Xu 1995); and (2) a deficiency of diffuse dust in M31, corresponding to a face-on V-band optical depth of $\tau_V \sim 0.3$ (Xu & Helou 1996, hereafter Paper II) which is more than a factor of 2 lower than the average face-on optical depth of Sb/Sc galaxies (Xu & Buat 1995). On the other hand, our results, showing that about 60% of the FIR (40–120 μm) emission of M31 is caused by diffuse dust not associated with H II regions, do not support the suggestion of Devereux et al. (1994) that the FIR emission of M31 is predominantly caused by ionizing stars.

6. SUMMARY

The high-resolution (HiRes) *IRAS* maps of the Andromeda galaxy (M31) are used to investigate the morphology of the infrared (IR) emission and the properties of discrete far-infrared (FIR) sources in its disk. Very thin and bright FIR arm segments are shown in these maps, which have similar structure as the H I gas but with much enhanced arm/interarm contrast, typically a factor of ~5 on the 60 μm image. We identify 39 unconfused sources (excluding the nucleus) and 14 confused sources (seven pairs) at 60 μm by direct Gaussian fitting to the image, with careful treatment of the source confusion problem. The *IRAS* colors of 10 bright isolated 60 μm sources are studied as a presumably representative sample of the discrete source population. They follow the well-known anticorrelation between $f_{60\,\mu m}/f_{10\,\mu m}$ and $f_{12\,\mu m}/f_{25\,\mu m}$, with mean *IRAS* colors $\langle f_{12\,\mu m}/f_{60\,\mu m}\rangle = 0.14 \pm 0.02$, $\langle f_{25\,\mu m}/f_{60\,\mu m}\rangle = 0.19 \pm 0.02$, and $\langle f_{60\,\mu m}/f_{100\,\mu m}\rangle = 0.30 \pm 0.04$. All sources except the nucleus coincide with optical H II regions. A comparison with Hα observations shows that the total luminosity (in the wavelength range 8–1000 μm) associated with H II regions is $7.2 \pm 2.19 \times 10^8\ L_\odot$, namely, 30% ± 14% of the total IR emission of M31. This is a factor of 3.6 greater than the IR luminosity of the warm component of Walterbos & Schwering (1987). However, our result does not agree with the suggestion of Devereux et al. (1994) that the FIR emission of M31 is predominantly energized by high-mass stars. About half the IR luminosity of the H II region–associated component emerges from discrete FIR sources. The luminosity translates into a present day star formation rate of $0.36 \pm 0.14\ M_\odot$ yr^{-1}, about an order of magnitude lower than that of the Milky Way.

We are very grateful to E. Brinks for providing the H map of M31. We are indebted to the referee, R. Walterbos, whose comments helped to improve this paper in various aspects. Helpful discussions with C. Beichman, E. Berkhuijsen, and J. Fowler are acknowledged. Part of the work was done when C. X. was at Max-Planck-Institut für Radioastronomie, supported by an Alexander von Humboldt Fellowship. He thanks Professor R. Wielebinski for his hospitality. This research is supported in part through the *IRAS* Extended Mission Program by the Jet Propulsion Laboratory, California Institute of Technology, under a contract with the National Aeronautics and Space Administration. C. X. acknowledges that part of the work in this paper has been done within the framework of the Sonderforschungsberich 328 (Entwicklung von Galaxien) of the Deutsche Forschungsgemeinschaft.

REFERENCES

Aumann, H. H., Fowler, J. W., & Melnyk, M. 1990, AJ, 99, 1674
Berkhuisjen, E. M., Wielebinski, R., & Beck, R. 1983, A&A, 11, 141
Bloemen, J. B. G. M., Duel, E. R., & Thaddeus, P. 1990, A&A, 233, 437
Boulanger, F., Beichman, C., Désert, F. X., Helou, G., Pérault, M., & Ryter, C. 1988, ApJ, 332, 328
Brinks, E. 1984, Ph.D. thesis, Univ. Leiden
Brinks, E., & Shane, W. W. 1984, A&AS, 55, 179
Buat, V., & Xu, C. 1995, A&A, in press
Cox, P., Krügel, E., & Mezger, P. G. 1986, A&A, 155, 380
Cox, P., Mezger, P. 1988, in Lecture Notes in Physics 297, Comets to Cosmology, ed. A. Lawrence (Heidelberg: Springer), 97
Désert, F. A., Boulanger, F., & Puget, J. L. 1990, A&A, 273, 215
Devereux, N. A., Price, R., Wells, L. A., Duric, N. 1994, AJ, 108, 1667
Eadie, W. T., Drijard, D., James, F. E., Roos, M., & Sadoulet, B. 1977, Statistical Methods in Experimental Physics (Amsterdam: North-Holland)
Fowler, J. H., & Aumann, H. H. 1993, in Science with High Spatial Resolution, Far-Infrared Data, ed. S. Terebey & J. Mazzarella (Pasadena: Jet Propulsion Laboratory), 1

Habing, H., et al. 1984, ApJ, 278, L59
Helou, G. 1986, ApJ, 311, L33
Helou, G., Khan, I. R., Malek, LL., & Beohmer, L. 1988, ApJS, 68, 151
Helou, G., Ryter, C., Soifer, B. T. 1991, ApJ, 376, 505
Kennicutt, R. C. 1984, ApJ, 287, 116
———. 1992, ApJ, 388, 310
Kennicutt, R. C., Edgar, B. K., & Hodge, P. W. 1989, ApJ, 337, 761
Mezger, P. G. 1988, in Galactic and Extragalactic Star Formation, ed. R. E. Pudritz and M. Fich (Dordrecht: Kluwer), 227
Pellet, A., Astier, N., Viale, A., Courtés, G., Maucherat, A., Monnet, G., & Simien, F. 1978, A&AS, 31, 439
Pérault, M., Boulanger, F., Puget, J. L., & Falgarone, E. 1989, unpublished
Rice, W. 1993, AJ, 105, 67
Rice, W., Boulanger, F., Viallefond, F., Soifer, B. T., & Freedman, W. L. 1990, ApJ, 358, 418
Soifer, B. T., Rice, W. L., Mould, J. R., Gillet, F. C., Rowan-Robinson, M., & Habing, H. J. 1986, ApJ, 304, 651
Thronson, H. A., & Telesco, C. M. 1986, ApJ, 311, 98
Walterbos, R. A. M. 1988, in Galactic and Extragalactic Star Formation, ed. R. E. Pudritz & M. Fich (Dordrecht: Kluwer), 361
Walterbos, R. A. M., & Braun, R. 1992, A&AS, 92, 625 (WB92)
———. 1994, ApJ, 431, 156
Walterbos, R. A. M., & Kennicutt, R. C. 1987, A&AS, 69, 311
Walterbos, R. A. M., & Schwering, P. B. W. 1987, A&A, 180, 27 (WS87)
Xu, C. 1990, ApJ, 365, L47
Xu, C., & Buat, V. 1995, A&A, 293, L65
Xu, C., & Helou, G. 1993, in Science with High Spatial Resolution Far-Infrared Data, ed. S. Terebey & J. Mazzarella (Pasadena: Jet Propulsion Laboratory), 87
———. 1994, ApJ, 426, 109
———. 1995, ApJ, 446, 909 (erratum)
———. 1996, ApJ, 456, 163 (Paper II)
Xu, C., Klein, U., Meinert, D., Wielebinski, R., & Haynes, R. F. 1992, A&A, 257, 47